REPORT DOCUMENTATION PAGE

Form Approved OMB NO. 0704-0188

The public reporting burden for this collection of information is estimated to average 1 hour per response, including the time for reviewing instructions, searching existing data sources, gathering and maintaining the data needed, and completing and reviewing the collection of information. Send comments regarding this burden estimate or any other aspect of this collection of information, including suggesstions for reducing this burden, to Washington Headquarters Services, Directorate for Information Operations and Reports, 1215 Jefferson Davis Highway, Suite 1204, Arlington VA, 22202-4302. Respondents should be aware that notwithstanding any other provision of law, no person shall be subject to any oenalty for failing to comply with a collection of information if it does not display a currently valid OMB control number.
PLEASE DO NOT RETURN YOUR FORM TO THE ABOVE ADDRESS.

1. REPORT DATE (DD-MM-YYYY)	2. REPORT TYPE	3. DATES COVERED (From - To)
05-08-2012	Final Report	23-Mar-2009 - 22-Mar-2012

4. TITLE AND SUBTITLE

Broadband Electric-Field Sensor Array Technology

5a. CONTRACT NUMBER

W911NF-09-1-0073

5b. GRANT NUMBER

5c. PROGRAM ELEMENT NUMBER

611102

6. AUTHORS

Ronald M. Reano

5d. PROJECT NUMBER

5e. TASK NUMBER

5f. WORK UNIT NUMBER

7. PERFORMING ORGANIZATION NAMES AND ADDRESSES

Ohio State University Research Foundation
Office of Sponsored Programs
Ohio State University Research Foundation
Columbus, OH 43210 -1063

8. PERFORMING ORGANIZATION REPORT NUMBER

9. SPONSORING/MONITORING AGENCY NAME(S) AND ADDRESS(ES)

U.S. Army Research Office
P.O. Box 12211
Research Triangle Park, NC 27709-2211

10. SPONSOR/MONITOR'S ACRONYM(S)

ARO

11. SPONSOR/MONITOR'S REPORT NUMBER(S)

52603-EL-YIP.6

12. DISTRIBUTION AVAILIBILITY STATEMENT

Approved for Public Release; Distribution Unlimited

13. SUPPLEMENTARY NOTES

The views, opinions and/or findings contained in this report are those of the author(s) and should not contrued as an official Department of the Army position, policy or decision, unless so designated by other documentation.

14. ABSTRACT

We report the development of a broadband electric field sensor array technology to detect radio frequency (RF) electromagnetic energy. An approach based on planar electro-optical resonators is considered. We have developed sensors based on electro-optic polymers and sensors based on a hybrid material system consisting of silicon and lithium niobate. Test and measurement of fabricated sensors based on disperse red one electro-optic polymers yielded a sensitivity of 95 Volts per meter per root Hertz in a footprint of 170 micrometers by 270 micrometers.

15. SUBJECT TERMS

Electric Field Sensors, Electro-optics

16. SECURITY CLASSIFICATION OF:			17. LIMITATION OF ABSTRACT	15. NUMBER OF PAGES	19a. NAME OF RESPONSIBLE PERSON
a. REPORT	b. ABSTRACT	c. THIS PAGE			Ronald Reano
UU	UU	UU	UU		19b. TELEPHONE NUMBER: 614-247-7204

Report Title

Broadband Electric-Field Sensor Array Technology

ABSTRACT

We report the development of a broadband electric field sensor array technology to detect radio frequency (RF) electromagnetic energy. An approach based on planar electro-optical resonators is considered. We have developed sensors based on electro-optic polymers and sensors based on a hybrid material system consisting of silicon and lithium niobate. Test and measurement of fabricated sensors based on disperse red one electro-optic polymers yielded a sensitivity of 95 Volts per meter per root Hertz in a footprint of 170 micrometers by 270 micrometers. The sensor based on hybrid silicon and lithium niobate was both more sensitive and more miniature. The demonstrated sensitivity was 4.5 Volts per meter per root Hertz and the footprint was 40 micrometers by 40 micrometers. We conclude that electro-optical resonators based on a hybrid material system of silicon and lithium niobate is a promising technology for broadband electric field sensor arrays. The results of this research program advance the state-of-the-art in electric field sensors with a host of applications including electromagnetic compatibility (EMC) measurements, high-frequency electronic circuit diagnostics, medical equipment field monitoring, radio-frequency reception, and high power microwave detection.

Enter List of papers submitted or published that acknowledge ARO support from the start of the project to the date of this printing. List the papers, including journal references, in the following categories:

(a) Papers published in peer-reviewed journals (N/A for none)

Received	Paper
2012/02/14 2: 4	Li Chen, Ronald M. Reano. Compact electric field sensors based on indirect bonding of lithium niobate to silicon microrings, Optics Express, (02 2012): 0. doi: 10.1364/OE.20.004032
2011/08/30 2: 1	Alexander C. Ruege, Ronald M. Reano. Sharp Fano Resonances From a Two-Mode Waveguide Coupled to a Single-Mode Ring Resonator, Journal of Lightwave Technology, (10 2010): 2964. doi: 10.1109/JLT.2010.2075913

TOTAL: 2

Number of Papers published in peer-reviewed journals:

(b) Papers published in non-peer-reviewed journals (N/A for none)

Received	Paper

TOTAL:

Number of Papers published in non peer-reviewed journals:

(c) Presentations

Number of Presentations: 0.00

Non Peer-Reviewed Conference Proceeding publications (other than abstracts):

Received	Paper

TOTAL:

Number of Non Peer-Reviewed Conference Proceeding publications (other than abstracts):

Peer-Reviewed Conference Proceeding publications (other than abstracts):

Received		Paper
2012/08/04 1	5	Li Chen, Ronald M. Reano. Electric Field Sensors based on Hybrid Silicon and Lithium Niobate Microring Resonators, Conference on Lasers and Electro-optics (CLEO). 2012/05/06 00:00:00, . : ,
2011/08/30 2	2	Alexander C. Ruege, Ronald M. Reano. Realization of near optimally sharp lineshapes from a two-mode-coupled single-mode ring resonator, 2010 23rd Annual Meeting of the IEEE Photonics Society (Formerly LEOS Annual Meeting). 2010/11/07 00:00:00, Denver, CO, USA. : ,

TOTAL: 2

Number of Peer-Reviewed Conference Proceeding publications (other than abstracts):

(d) Manuscripts

Received	Paper

TOTAL:

Number of Manuscripts:

Books

Received	Paper

TOTAL:

Patents Submitted

Patents Awarded

Awards

Graduate Students

NAME	PERCENT_SUPPORTED	Discipline
Alexander Ruege	0.25	
FTE Equivalent:	**0.25**	
Total Number:	**1**	

Names of Post Doctorates

NAME	PERCENT_SUPPORTED
FTE Equivalent:	
Total Number:	

Names of Faculty Supported

NAME	PERCENT_SUPPORTED	National Academy Member
Ronald M. Reano	0.00	
FTE Equivalent:	**0.00**	
Total Number:	**1**	

Names of Under Graduate students supported

NAME	PERCENT_SUPPORTED
FTE Equivalent:	
Total Number:	

Student Metrics

This section only applies to graduating undergraduates supported by this agreement in this reporting period

The number of undergraduates funded by this agreement who graduated during this period:	0.00
The number of undergraduates funded by this agreement who graduated during this period with a degree in science, mathematics, engineering, or technology fields:	0.00
The number of undergraduates funded by your agreement who graduated during this period and will continue to pursue a graduate or Ph.D. degree in science, mathematics, engineering, or technology fields:	0.00
Number of graduating undergraduates who achieved a 3.5 GPA to 4.0 (4.0 max scale):	0.00
Number of graduating undergraduates funded by a DoD funded Center of Excellence grant for Education, Research and Engineering:	0.00
The number of undergraduates funded by your agreement who graduated during this period and intend to work for the Department of Defense	0.00
The number of undergraduates funded by your agreement who graduated during this period and will receive scholarships or fellowships for further studies in science, mathematics, engineering or technology fields:	0.00

Names of Personnel receiving masters degrees

NAME
Total Number:

Names of personnel receiving PHDs

NAME
Alexander Ruege
Total Number: 1

Names of other research staff

NAME	PERCENT_SUPPORTED
FTE Equivalent:	
Total Number:	

Sub Contractors (DD882)

Inventions (DD882)

Scientific Progress

See Attachment

Technology Transfer

Final Report
Army Research Office Young Investigator Program
23 March 2009 to 22 March 2012

Broadband Electric-Field Sensor Array Technology

Ronald M. Reano, Associate Professor
Department of Electrical and Computer Engineering, Ohio State University
205 Dreese Laboratory, 2015 Neil Ave, Columbus, Ohio 43210 USA
Email: reano@ece.osu.edu

ABSTRACT
We report the development of a broadband electric field sensor array technology to detect radio frequency (RF) electromagnetic energy. An approach based on planar electro-optical resonators is considered. We have developed sensors based on electro-optic polymers and sensors based on a hybrid material system consisting of silicon and lithium niobate. Test and measurement of fabricated sensors based on disperse red one electro-optic polymers yielded a sensitivity of 95 Volts per meter per root Hertz in a footprint of 170 micrometers by 270 micrometers. The sensor based on hybrid silicon and lithium niobate was both more sensitive and more miniature. The demonstrated sensitivity was 4.5 Volts per meter per root Hertz and the footprint was 40 micrometers by 40 micrometers. We conclude that electro-optical resonators based on a hybrid material system of silicon and lithium niobate is a promising technology for broadband electric field sensor arrays. The results of this research program advance the state-of-the-art in electric field sensors with a host of applications including electromagnetic compatibility (EMC) measurements, high-frequency electronic circuit diagnostics, medical equipment field monitoring, radio-frequency reception, and high power microwave detection.

TABLE OF CONTENTS **PAGE**

I. Introduction 3

II. Theory 4

III. Electro-optic polymer sensors

III.A. Design 6

III.B. Fabrication 6

III.C. Test and measurement 8

IV. Hybrid silicon and lithium niobate sensors

IV.A. Design 12

IV.B. Fabrication 14

IV.C. Test and measurement 15

V. Conclusions 17

VI. References 19

I. INTRODUCTION

Advances in electric field sensors are important for a host of applications including electromagnetic compatibility (EMC) measurements, high-frequency electronic circuit diagnostics, medical equipment field monitoring, radio-frequency reception, and high power microwave detection.[1,2,3,4,5] In the case of electric field sensors based on the linear electro-optic (Pockels) effect, a high-frequency (DC to THz) electric field modifies the indices of refraction of an electro-optic medium, resulting in high-speed modulation of an optical carrier signal. Electric field sensors based on optical technology are advantageous, compared to electronic technology, because they can be metal free, compact, and broadband.[6] Furthermore, optical technology is amenable to realizing high spatial resolution sensor arrays and signal routing can utilize fiber optics.

Our vision for an electric field sensor array technology for the measurement of the magnitude and phase of electric-fields in RF/millimeter-wave circuits is shown in Fig. 1. The proposed measurement system is configured for frequency domain measurements. Compared to current techniques, this system possesses several advantages. First, a vector network analyzer (VNA) is inherent to this system. This enhances the probability of widespread acceptance of this technique within the microwave community. Second, since the optical beam is always in a guided-mode, virtually no optical alignment is necessary (once the system is configured), and therefore the system exhibits a high degree of ease-of-use. Third, the system does not require expensive waveplates and polarizers, reducing cost and alignment issues. Fourth, a continuous-wave laser is used in conjunction with a fast photodiode. This is a significantly more stable and economic configuration when compared with systems based on ultra-fast lasers and harmonic mixing schemes. The speed of the photodiode determines the measurement bandwidth (60 GHz photodetectors are commercially available). Fifth, use of an optical high-Q waveguide/cavity enables high-sensitivity probes with designer sensitivities. Finally, the configuration is inherently parallelizable. Using an array of sensors, mechanical translation of a point measurement probe, which is inherently slow and noisy, is eliminated.

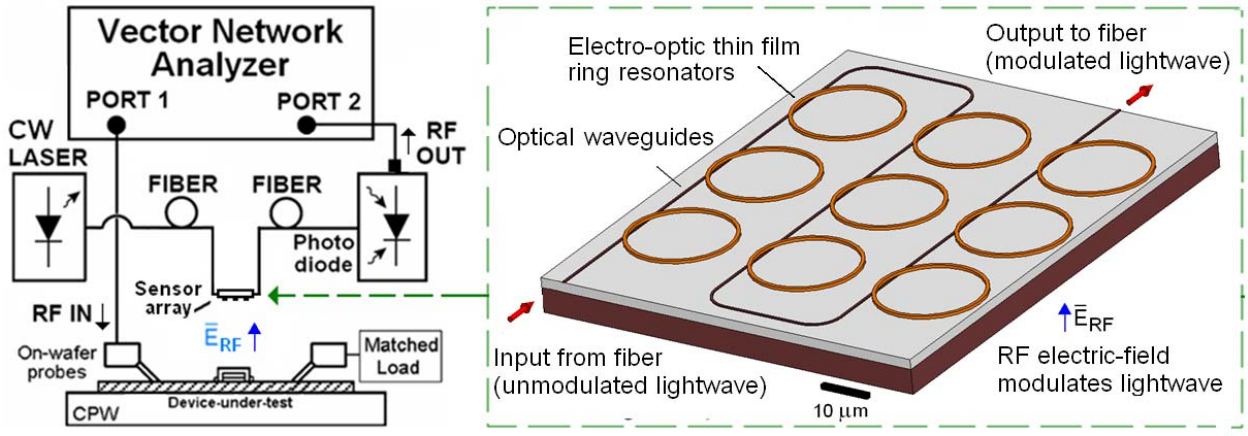

Fig. 1. Vision for electric field sensor array technology.

The measurement system operates as follows. Port-1 of a vector network analyzer (VNA) drives the RF/millimeter-wave device-under test (DUT). Unmodulated lightwaves from a tunable continuous wave (CW) laser source are coupled into an optical fiber that feeds the

sensor array. Light propagates along a planar optical waveguide that is coupled to the electro-optic ring resonator cavities. Each sensor element is addressed by tuning the CW laser source to within its resonance. Fringing electric-fields from the DUT modify the index of refraction of the electro-optic media in each ring, producing an amplitude modulation on the optical beam. The modulated lightwave is out-coupled to an optical fiber which is terminated in a high-speed photodiode. The demodulated RF signal is fed into port-2 of the VNA yielding measurements of the magnitude and phase of the RF electric-field. By sequentially tuning the laser source to within each resonance, a field map of the RF electric-field is obtained.

II. THEORY

The electric field sensor consists of a single-mode bus waveguide coupled to a single-mode ring-racetrack resonator. Laser light in the bus waveguide evanescently couples into the ring and generates resonant modes at distinct laser light wavelengths. The optical transmission spectra exhibits Lorentzian dips at the resonant wavelengths. From coupled mode theory the normalized power transmission can be expressed as[7,8]

$$T = 1 - \frac{\left(1-|t|^2\right)\left(1-\alpha_r{}^2\right)}{\left(1-|t|\alpha_r\right)^2 + 4|t|\alpha_r \sin^2\left(\varphi/2\right)} \tag{1}$$

The transmission coefficient of the optical field in the bus waveguide through the coupling region is t. The round-trip field transmission of the ring is α_r. The ring mode phase is $\varphi = 2\pi n_{eff} L_r / \lambda$ where the ring circumference is L_r, the effective index of the ring mode is n_{eff}, and the wavelength is λ. The resonance condition occurs for wavelengths corresponding to a ring phase that is an integer multiple of 2π and is, for integer m

$$\lambda_r = n_{eff} L_r / m \tag{2}$$

The laser wavelength, λ, is biased on the steep slope of the resonance. The resonance wavelength depends on the refractive index of the core, n_c, according to (2) because n_{eff} depends on n_c. An external RF electric field produces an electric field internal to the ring waveguide core, E_y, that modulates n_c via the linear electro-optic (EO) effect. For the resonators that we consider, the modulation is proportional to the r_{33} EO coefficient of the core material and is given by

$$\Delta n_c \propto r_{33} \Delta E_y \tag{3}$$

for optical fields polarized parallel to the vertical direction (*y*). The ratio of the change in the effective index of the ring mode for a change in the core index is defined as $\eta \equiv dn_{eff} / dn_c$ where η is determined by the optical power confinement in the core.[9] It is assumed that η is constant for small Δn_c. The modification of n_{eff} thus modulates the resonance wavelength due to (2) by $d\lambda_r / dn_{eff} = \lambda_r / n_{eff}$ which produces an intensity modulation on the optical carrier. The change in normalized transmission at the bias wavelength is thus approximately

$$\Delta T \approx S(\lambda) \lambda_r \eta \Delta n_c / n_{eff} \tag{4}$$

The parameter $S(\lambda)$ is the slope of the ring resonator optical transmission spectrum with respect to wavelength at the bias wavelength. In deriving (4) it is assumed that Δn_c is small so that S is constant and the transmission spectrum given by (1) only undergoes a translation with respect to wavelength. The intensity-modulated output light is directed into a high-speed photodiode. The amplitude of the intensity modulation is given by $\Delta P = \Delta T P_{opt}$ where P_{opt} is the peak total optical power off resonance received by the photodiode. The intensity modulation is converted to an output voltage modulation on the output RF transmission line (impedance Z_0 = 50 Ω) via a transimpedance amplifier connected to the photodiode. The voltage amplitude is $\tilde{V} = G\Delta P$ where G is the conversion gain of the photodiode and amplifier. The RF power detected by an RF receiver with a matched impedance is $P_{rf} = |\tilde{V}|^2/(2Z_0)$. The RF power due to EO modulation is thus

$$P_{rf} = \frac{\left[GS(\lambda)\eta P_{opt}\lambda n_c^3 r_{33}\Delta E_y\right]^2}{8Z_0 n_{eff}^2} \tag{5}$$

The slope S is determined by the ring waveguide loss characterized by α_r and the coupling between the ring waveguide and bus waveguide characterized by t. For resonators with larger loaded quality factors Q_L, the maximum achievable S is therefore larger. To maximize S for a fixed ring loss the coupling should be optimized for the ring resonator. From numerical simulations[10], the maximum lineshape slope occurs for under-coupled resonator and an extinction ratio of 9. To obtain this coupling condition t is related to α_r by

$$|t| \approx (3\alpha_r + 1)/(\alpha_r + 3) \tag{6}$$

The RF power obtained by EO modulation from a resonator as a function of wavelength is calculated using (1) and (5) and is shown in Fig. 2. The maxima of the RF power correspond

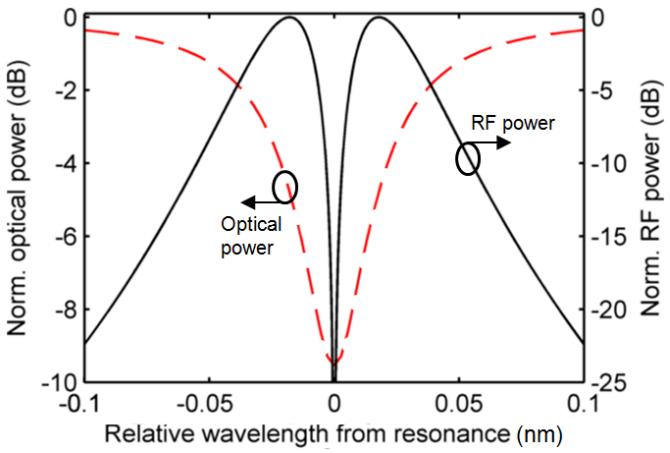

Fig. 2. Calculated normalized optical power and RF power due to EO modulation for a ring resonator. The RF power is largest at the steepest points on the resonance lineshape. The calculation is performed for α_r = 0.94 and $|t|$ = 0.97.

to the steepest points on the lineshape slope of the optical transmission. The laser wavelength should be biased at one of these points to maximize P_{rf}. At resonance, the modulated RF power is zero. The phase of the RF signal on the blue side of the resonance is 180° out of phase with the red side because of the opposite signs of the slope of the optical transmission.

III. ELECTRO-OPTIC POLYMER SENSORS

III.A. DESIGN

Integrated optical sensors supported by thin, flexible polymer substrates are desirable because they have low invasiveness to the sensed RF fields and may conform to the device-under-test (DUT).[11,12] We have designed a miniature ring resonator electro-optic (EO) polymer electric field sensor based on an all-polymer platform. A schematic of the sensor is shown in Fig. 3. The sensor is realized on a low-dielectric constant flexible polymer (SU-8, ε_r = 3.2) that is 30 μm thick. The waveguide cores consist of polycarbonate (PC, ε_r = 3.0) polymer doped with Disperse Red 1 (DR1) EO chromophore. The waveguide cores are embedded in fluorinated polymer Cytop (ε_r = 2.0) cladding.[13]

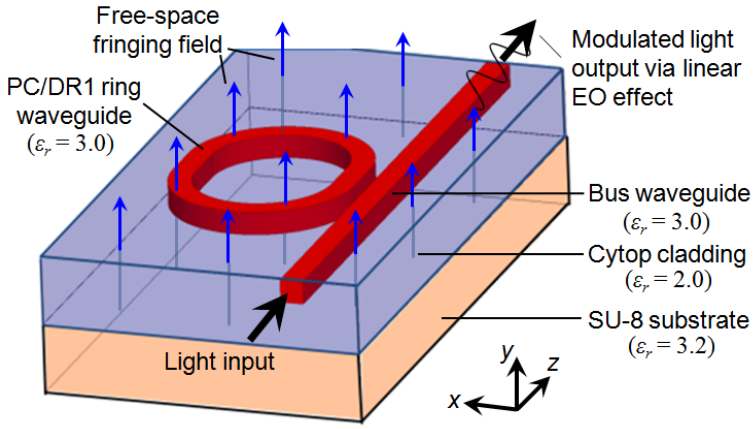

Fig. 3. All-polymer electric field sensor on flexible substrate.

III.B. FABRICATION

The fabrication process of the EO ring resonator is designed to fulfill two requirements: perform vertical field poling with electrodes as close as possible to the waveguides and fabricate a completely metal-free device. The ring resonator geometry is designed using the three-dimensional beam-propagation method. The commercially available EO chromophore DR1 is used for proof-of concept purposes.

PC/DR1 waveguide cores that are 1 μm tall are fabricated on top of a chromium (Cr) electrode. The Cr is deposited on thermally grown SiO_2 on a silicon (Si) wafer. The width and height of all waveguides is equal to 1.5 μm and 1.0 μm respectively. The waveguides are patterned using an ultraviolet (UV) photolithographic lift-off process and are covered by a 3.7 μm-thick layer of Cytop deposited by spin-coating. The fluorinated solvent does not attack the PC/DR1 structures during spin-coating.

An aluminum top electrode is next deposited on the Cytop. The sample is poled by applying 200 V between the two electrodes for five minutes at 150 °C, near the glass transition temperature of PC (T_g = 155 °C). After poling, the top electrode is removed in a wet chemical

etch. The poled sample at this step is schematically shown in Fig. 4(a). A 30 μm-thick layer of SU-8 2025 is coated on the Cytop and patterned by UV photolithography. The Cytop is resistant to attack by the SU-8 solvent and the SU-8 developer solvent. The PC/DR1 ridges are also protected by the Cytop and are not adversely affected by the solvents used during fabrication. A schematic of this step is shown in Fig. 4(b). The patterned area of the SU-8 defines the area of the sensor substrate. Reduction of the EO coefficient is minimized by exposing the poled sample to a maximum temperature of 60 ^{o}C during the SU-8 patterning step.

The SU-8 is used as an etch mask during the dry etch of Cytop and PC/DR1 using an oxygen chemistry. Fig. 4(c) is a schematic of the sample after the etch step. The waveguide in- and out-coupling facets are defined at this etch step. Finally, the etched sample is released from the Cr film in a hydrofluoric acid bath. The device is depicted in the schematic of Fig. 4(d). The released sensor is flexible and completely metal free. The total thickness of the SU-8 substrate and waveguide layer is 33.7 μm. Fig. 5 is a photograph showing the released device that is 8.4 mm long and 1.3 mm wide. The SU-8 is transparent to visible light allowing accurate positioning of the sensors over an RF DUT. The inset is a photomicrograph of fabricated four-ring sensor arrays. The length of the array is 1.2 mm. The ring resonators have a radius of 85 μm.

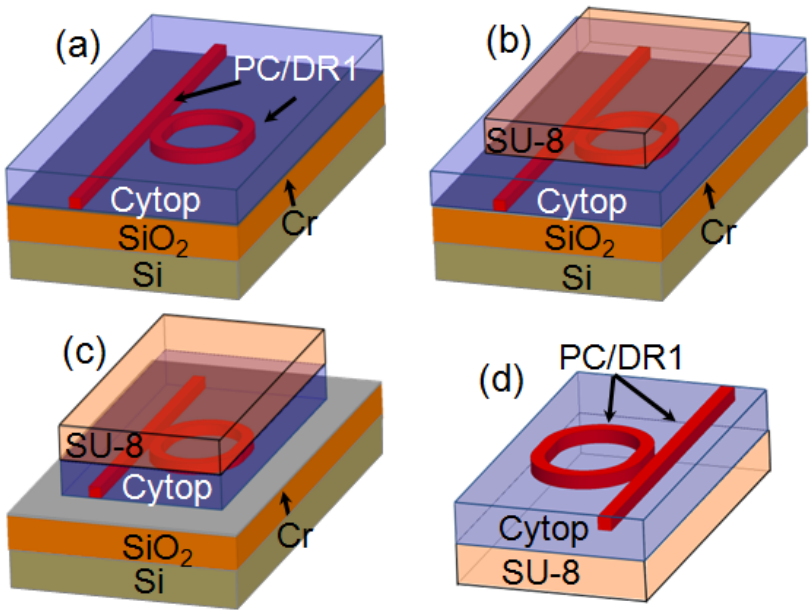

Fig. 4. (a) Poled PC/DR1 ridges embedded in Cytop on top of the Cr electrode that is supported by the SiO_2 on Si. The top electrode has been removed in the previous step. (b) Deposited and patterned SU-8 performed by UV photolithography. (d) The Cytop and PC/DR1 ridges are etched in a dry oxygen plasma using the SU-8 as a mask. (e) Released sample.

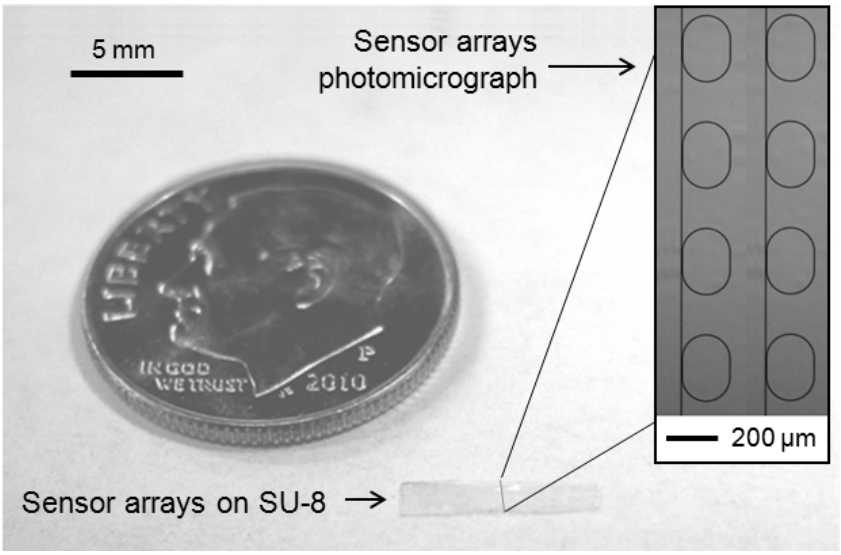

Fig. 5. Fabricated array of ring resonators on SU-8 substrate, relative to size of a dime. The sensor is 8.4 mm long, 1.3 mm wide and 35 μm thick. Inset: photomicrograph of four-ring sensor arrays. The length of the array is 1.2 mm.

III.C. TEST AND MEASUREMENT

The schematic of the laboratory test configuration is shown in Fig. 6(a). Light from a continuous wave (CW) tunable near-infrared laser amplified by an erbium-doped fiber amplifier (EDFA) is guided by single-mode optical fiber and coupled into and out of the waveguide devices via tapered fibers. The fibers are butt-coupled against the waveguide facets. The polarization of the light is set to TM by a polarization controller. The output light is directed into a high speed photoreceiver (G = 900 V/W). The RF source supplies power to the RF DUT. The RF receiver measures the power output from the photodiode, P_{rf}.

Fringing RF electric fields from a microstrip resonator circuit are measured by placing the ring resonators on top of the circuit. A photograph of the microstrip resonator circuit is shown in Fig. 6(b). The circuit is a one port device and consists of a 50 Ω input line gap-coupled to a second 50 Ω microstrip line resonator. From vector network analyzer (VNA) S_{11} measurements, the return loss from the second resonance at 3.9 GHz is -8.2 dB. The sensor arrays are positioned on the edge of the coupled microstrip line, where the electric field is largest at the resonance frequency as calculated by finite element method simulations using HFSS (ANSYS, Inc.). The vertical electric field in the ring waveguide core is estimated by calculating the RF electric field in air above the circuit, averaging over a region where the ring resonators are to be positioned, and then dividing by ε_r = 3.0. The vertical field in the core is at most 8.7 kV/m for 1 W RF input power at 3.9 GHz.

For the EO sensing tests the VNA acts as the RF source and RF receiver. Port one is connected to an RF amplifier. The output of the RF amplifier is connected to the RF microstrip circuit. The RF output of the photoreceiver is connected to port two of the VNA. A power of 1 W at 3.9 GHz is applied to the RF resonator and the magnitude and phase of S_{21} is measured. The optical power input to the ring resonator devices is 14.5 dBm. The laser wavelength is swept across a ring resonance wavelength at 1551.14 nm from one of the four resonators in the linear array. Fig. 7(a) shows the optical power transmission spectra. The

measured Q_L is 20,000 and the extinction ratio is 9.0 dB. Fig. 7(b) shows the measured magnitude of S_{21} as a function of laser wavelength. Two peaks in the data are observed and occur at the steepest points on the lineshape of Fig. 7(a). The maximum magnitude of S_{21} in Fig. 7(b) is -93 dB. The magnitude of S_{21} is also at a minimum when the laser wavelength is at ring resonance. The phase of S_{21} is shown in Fig. 7(c). At ring resonance, a phase shift of approximately 180° is observed. Note the similarity of the data of Figs. 7(b) and (c) and the theoretical results shown in Fig. 2.

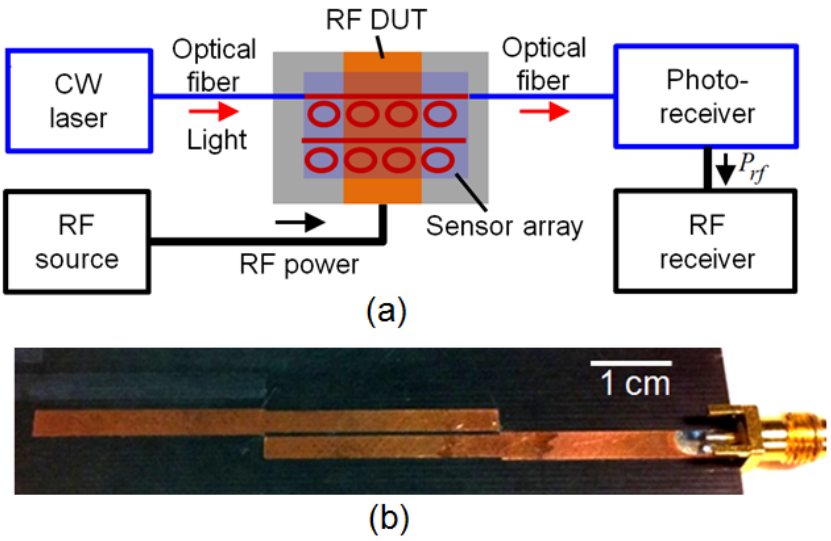

Fig. 6. (a) Schematic of the laboratory test configuration. The sensor array is placed directly on top of the RF device-under-test (DUT). The modulated laser light from the sensor is input to the photoreceiver, which is connected to the RF receiver. (b) Photograph of the RF microstrip resonator used for EO testing. The circuit is constructed on a Rogers Duroid 5880 substrate.

The modulation from the ring resonator is measured as a function of RF frequency at a laser wavelength of 1551.19 nm. An input power of 1 mW is applied to the RF resonator. The optical power and fiber coupling is adjusted so that the power incident at the photodiode is -2 dBm. Fig. 8 shows the measured magnitude of S_{21} from 3.65 GHz to 4.1 GHz. The signal at resonance is -97 dB and is 8 dB higher than the highest noise power measured off-resonance.

To demonstrate sensing via wavelength multiplexing of the four-ring array, the laser wavelength is swept across the four resonances. The resonators are designed to be nominally the same. Small fabrication differences between the resonators created resonance wavelength separation in the transmission spectra. The measured magnitude and phase of S_{21} are shown in Fig. 9(a) and (b) respectively. There are two peaks in the magnitude of S_{21} near each resonance located at 1550.80 nm, 1551.18 nm, 1551.51 nm, and 1551.61 nm. The phase shift from the blue side to the red side in the spectra at each resonance is approximately 180°. Each resonance corresponds to a different location on the sensor array. The magnitude and phase of S_{21} measured for each resonance can then be used to determine the electric field magnitude and phase inside of the ring.

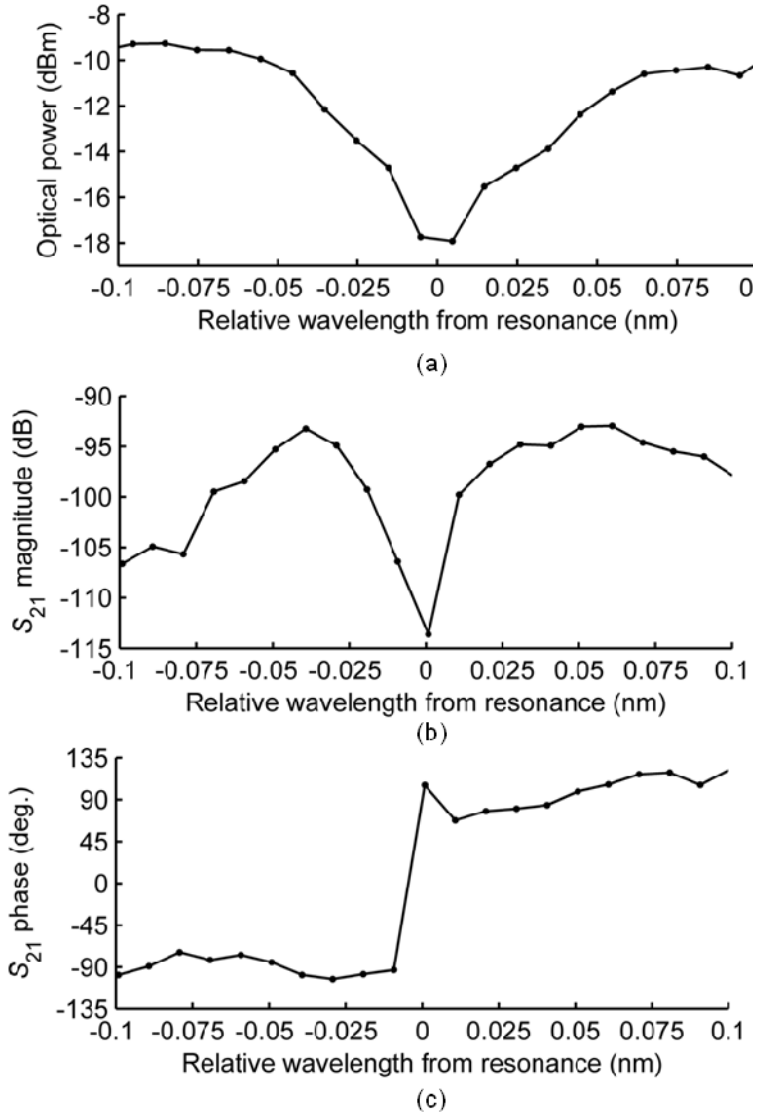

Fig. 7. (a) Optical power transmission spectra for the S_{21} EO measurements. The resonance wavelength is 1551.14 nm. (c) Magnitude of S_{21} as the laser wavelength is swept across ring resonance wavelength. The laser wavelength is stepped by 0.01 nm and is held constant for 2.5 seconds at each wavelength point. The VNA is set to a 10 Hz IF bandwidth and 7 point averaging. (d) The measured phase of S_{21}. Note the phase shift of approximately 180^o near ring resonance.

The field sensitivity is estimated using the measured data of Fig. 7 and equation (5). The sensitivity is defined as the minimum detectable electric field magnitude, internal to the ring waveguide core, for a signal-to-noise ratio of 1 using a measured VNA noise level of -122 dB (8 dB above the rms noise). The intermediate frequency bandwidth is 10 Hz. The normalized slope S is 12.1 inverse nm. From the effective index method for n_c =1.58, η = 0.8 and n_{eff} = 1.43. The maximum optical transmission power is P_{opt} = -9 dBm. Therefore, the sensitivity calculates to approximately 95 V m^{-1} Hz$^{-1/2}$.

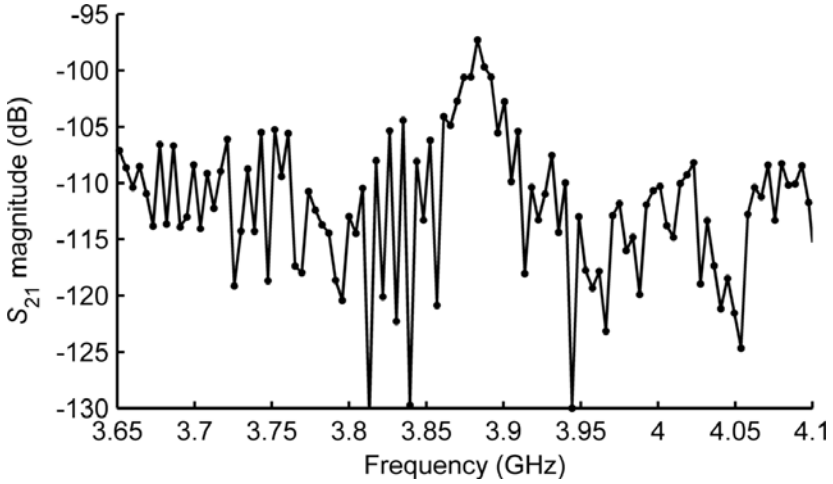

Fig. 8. Measured S_{21} magnitude as a function of RF frequency near the second resonance of the RF resonator. The laser wavelength is held constant at 1551.19 nm. The VNA is set to a 10 Hz IF bandwidth. Three frequency sweeps are averaged.

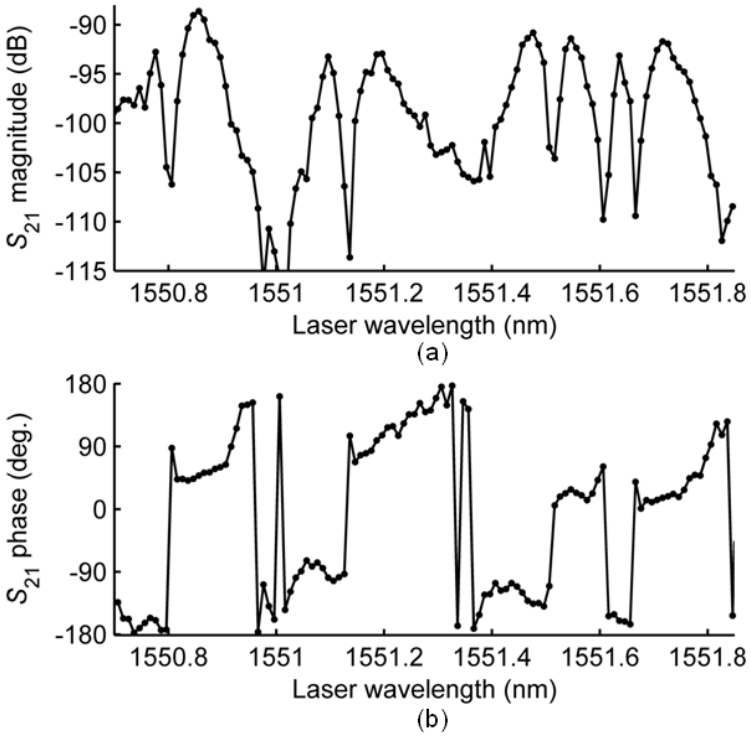

Fig. 9. (a) Magnitude of S_{21} as the laser wavelength is swept across ring resonance wavelengths of the four-ring array. The VNA settings are similar to those for the data shown in Fig. 8. The resonance wavelengths are 1550.80 nm, 1551.18 nm, 1551.51 nm, and 1551.61 nm. (b) The measured phase of S_{21} measured for the four-ring array.

IV. HYBRID SILICON AND LITHIUM NIOBATE SENSORS

IV.A. DESIGN

Submicrometer thin films of lithium niobate ($LiNbO_3$) are attractive for miniaturized electric field sensors because of the high optical confinement, large electro-optic coefficients, fast response time, and transparency at telecommunications wavelengths.[14,15] Structuring of the thin film into planar waveguide devices yields compact and high density integrated optics. The bend radius, however, is limited by the refractive index contrast between core and cladding. By comparison, the larger refractive index contrast in the silicon-on-insulator (SOI) material system enables waveguide bends with micrometer scale radii of curvature.[16] Unstrained crystalline silicon is, however, centrosymmetric. Therefore, it does not exhibit a linear electro-optic effect. A hybrid material system consisting of both SOI and $LiNbO_3$ enables compact integrated optics with functionality provided by second order susceptibility. Recent efforts in this direction include demonstrations of direct bonding of $LiNbO_3$ to SOI to realize compact high speed optical modulators and fast tuning of filters.[17] Generally, direct bonding of two materials involves the concatenation of two smooth and clean material interfaces without the use of an intermediate layer. Direct bonding typically requires very flat surfaces, demanding process technology, and specialized equipment. An alternative to direct bonding is indirect bonding. Indirect bonding of two materials involves the use of an intermediate layer such as polymer, spin-on-glass, or metal.[18] It is a robust and low temperature technique that is relatively insensitive to surface topography.[19]

In this section, the first demonstration of compact and metal-free electric field sensors based on the indirect bonding of submicrometer thin films of $LiNbO_3$ to silicon microring resonators are presented. An electric field sensor is designed and fabricated by utilizing a 600 nm thick z-cut $LiNbO_3$ ion-sliced thin film as the top cladding of a 20 μm radius silicon microring resonator. The optical quasi transverse magnetic (quasi-TM) mode is used to access the r_{33} electro-optic coefficient in the $LiNbO_3$ (r_{33} = 31 pm V^{-1}, r_{31} = 8 pm V^{-1} in bulk $LiNbO_3$).[20,21] The intermediate bonding layer is benzocyclobutene (BCB). Operation of the device as an electric field sensor is demonstrated by detecting the fringing fields from a microwave frequency microstrip circuit operating at 1.86 GHz.

A schematic of the hybrid Si/$LiNbO_3$ electric field sensor is shown in Fig. 10a. The sensor consists of a bus coupled SOI strip waveguide ring resonator and a thin film of $LiNbO_3$ which serves as a portion of the top cladding. The silicon waveguide core width is 450 nm and the height is 250 nm. The $LiNbO_3$ thin film is 600 nm thick and is bonded to the silicon resonator via BCB. The whole sensor is covered by one micrometer thick plasma enhanced chemical vapor deposition (PECVD) SiO_2. Figure 10b shows a scanning electron micrograph (SEM) of the cross-section of the sensor structure. A ring radius of 20 μm is chosen to avoid large bending losses.

An optical carrier signal propagating as a guided wave in the SOI bus waveguide is evanescently coupled into the ring resonator via a 375 nm wide coupling gap. A portion of the guided-mode is within the $LiNbO_3$ thin film. For optical wavelengths near the resonance wavelengths of the ring resonator, the optical transmission is sensitive to modulations in the effective index of the guided-mode in the ring resonator. The use of a high-Q resonator is desirable because the sensitivity depends on the slope of the optical transmission versus wavelength. When the sensor is immersed within a high-frequency electric field, the electric field can be detected because it modifies the refractive indices in the $LiNbO_3$ thin film via the

electro-optic effect. Consequently, the effective index of the guided-mode in the ring resonator is modulated, resulting in an intensity modulation of the optical carrier.

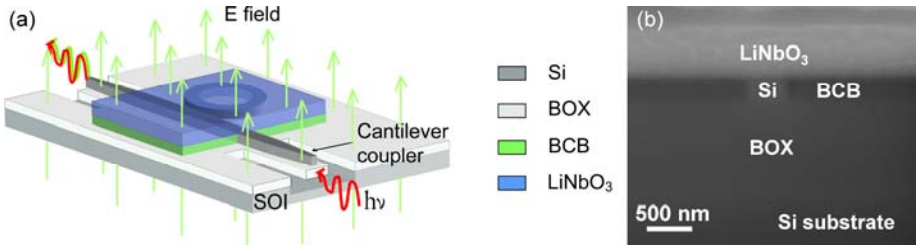

Fig. 10. (a) Schematic of an electric field sensor based on the indirect bonding of a lithium niobate thin film to a silicon microring resonator. For clarity, a PECVD SiO_2 top-cladding layer is not shown. (b) SEM of the cross-section of the sensor structure.

The optical polarization of the guided mode is chosen to maximize the fraction of the optical mode that overlaps with the $LiNbO_3$. Maximum overlap optimizes the change in the effective index of the optical mode that occurs for a change in the refractive indices of the $LiNbO_3$. Figure 11 shows the cross-section electric field distributions, for the quasi-TE and quasi-TM modes at 1550 nm optical wavelength, calculated using the beam propagation method (BPM). The effective index calculates to 2.33 for TM mode and 2.58 for TE mode. Since the TM mode is less confined, a larger fraction of the optical mode is in the $LiNbO_3$ for the TM mode than the TE mode. In addition, the TM mode accesses the r_{33} electro-optic coefficient of the $LiNbO_3$, whereas the TE mode accesses the r_{13} electro-optic coefficient. Therefore, the optical TM mode is chosen in the design. Compared to fabricated devices, the simulations shown in Fig. 11 neglect several tens of nanometers of BCB that resides on the top surface of the silicon core. The presence of BCB between the top of the silicon core and the bottom of the $LiNbO_3$ thin film results in a reduction of the TM mode electric field inside the $LiNbO_3$ due to the electromagnetic boundary conditions. Therefore, in order to maximize the fraction of the optical mode in the $LiNbO_3$, it is important to minimize the BCB thin film thickness that is directly on top of the silicon core.

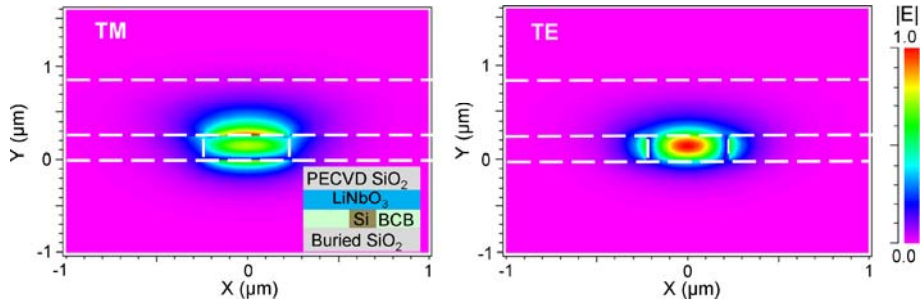

Fig. 11. Optical electric field distributions in the hybrid Si/$LiNbO_3$ sensor for the quasi-TM (E_y component) and quasi-TE (E_x component) modes at 1550 nm wavelength. Material boundaries are indicated by the white dashed lines and the material regions are indicated in the inset.

IV.B. FABRICATION

The fabrication process is shown in Fig. 12. The process begins with a SOI wafer. The thickness of the silicon device layer is 250 nm, the thickness of the buried oxide (BOX) is 1 μm, and the thickness of the silicon substrate is thinned to 210 μm. Silicon strip waveguides forming a silicon microring and a bus waveguide with inverse width tapers are defined in HSQ resist using electron-beam lithography and inductively coupled plasma reactive ion etching (ICP-RIE) using Cl_2/O_2 chemistry. The cross-sectional width and height of the silicon strip waveguides are 450 nm and 250 nm, respectively. The radius of the ring resonator is 20 μm and the coupling gap is 375 nm.

Thin films of $LiNbO_3$ are obtained from a bulk single crystal z-cut $LiNbO_3$ wafer using helium ion implantation and thermal treatment. The implantation energy is 195 keV and the fluence is 4×10^{16} ions cm^{-2}. After implantation, the wafer is annealed using rapid thermal annealing (RTA) and then etched in hydrofluoric acid (HF) solution.[22] Non-uniform stress produces 700 nm thick $LiNbO_3$ thin films in the areal shape of strips and triangles whose edges are formed along crystal planes. The edge length ranges from several tens of micrometers to several hundred micrometers. The surface roughness of the implanted side of the $LiNbO_3$ thin film is reduced to 4 nm by ICP etching with Ar chemistry resulting in a final film thickness of 600 nm.

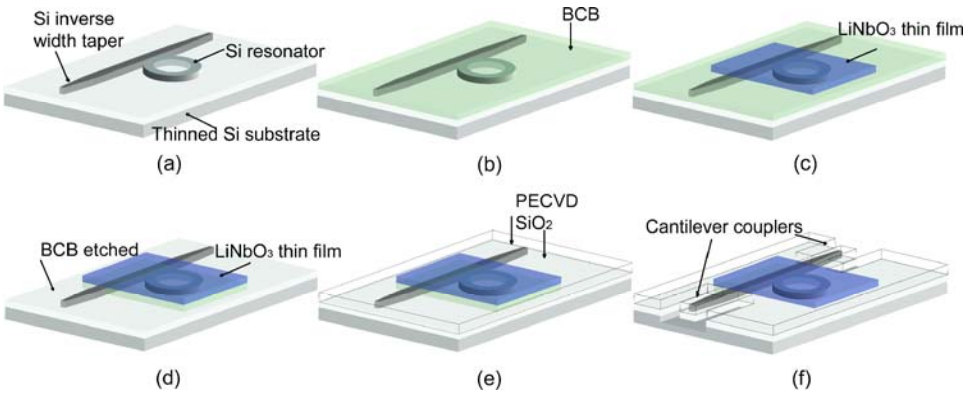

Fig. 12. Fabrication process of electric field sensor: (a) Silicon strip waveguide ring resonator patterned on SOI wafer using electron beam lithography and plasma etch, (b) spin-coat of BCB, (c) indirect bonding of $LiNbO_3$ thin film, (d) plasma etch of BCB, (e) deposition of PECVD SiO_2, (f) fabrication of cantilever couplers.

Next, BCB is spin-coated from solution onto the silicon strip waveguides. $LiNbO_3$ thin films are transferred to the top of the SOI ring resonators using a fiber tip on a probe station. After transfer, the sample is annealed to 300 °C to cure the BCB and to partially recover the r_{33} coefficient, resulting in a BCB layer approximately 20 nm thick between the $LiNbO_3$ and the silicon microring. The $LiNbO_3$ thin film does not crack after annealing despite the large mismatch in thermal expansion coefficients between silicon and $LiNbO_3$. BCB that is not covered by the $LiNbO_3$ thin film is etched using CF_4/O_2 ICP-RIE. A 1 μm thick SiO_2 top cladding is deposited by PECVD. Finally, cantilever couplers are fabricated for fiber coupling to the bus waveguide.[23] The bus waveguide, including the cantilever couplers, is 640 μm long.

IV.C. TEST AND MEASUREMENT

The electric field sensor is demonstrated in the laboratory by detecting fringing electric fields from a radio-frequency (RF) microstrip circuit. At a constant RF power, the RF electric field varies spatially above the circuit. By positioning the sensor at various points above the circuit, a field map of the electric field distribution can be obtained. The microstrip circuit is an RF coupled line resonator operating on resonance at 1.86 GHz with an RF return loss of 7.4 dB. The RF frequency of the circuit is well within the RF bandwidth of the sensor which is limited by the photon lifetime of the ring resonator.

The experimental setup is shown in Fig. 13 along with a top-view optical micrograph of the fabricated electric field sensor. In the demonstration, the chip is placed on the surface of the RF microstrip circuit in a region where the fringing electric field is a maximum. Port 1 of a calibrated microwave vector network analyzer (VNA) drives the RF microstrip circuit with 1 mW of RF power. An infrared continuous-wave laser source is connected to a polarization controller which outputs linearly polarized quasi-TM light with cross-polarization rejection ratio of more than 17 dB. Tapered optical fibers with tip diameter approximately equal to 2 μm are butt-coupled to the input and output cantilever couplers of the electric field sensor.

Fringing electric fields from the microstrip circuit modify the effective index of the optical mode in the electric field sensor, producing an intensity modulation on the optical beam. The modulated lightwave is out-coupled via optical fiber which is terminated in a high-speed photodiode with responsivity equal to 0.9 A/W and transimpedance gain equal to 1000 V/A, resulting in a photoreceiver conversion gain of 900 V/W. The demodulated RF signal is fed into port 2 of the VNA. The RF power entering port 2 is proportional to the square of the magnitude of the vertical component of the RF electric field in the $LiNbO_3$ portion of the sensor, weighted by the optical mode intensity distribution. Furthermore, the RF power entering port 2 is proportional to the square of the optical power and the square of the slope of the optical transmission versus wavelength. The microwave VNA is set to measure the port 1 to port 2 S_{21} scattering parameter. The square of the magnitude of S_{21}, $|S_{21}|^2$, is the RF power delivered to port 2 normalized by the RF power available from port 1. The VNA operates with an intermediate frequency (IF) bandwidth of 10 Hz and 20 averages.

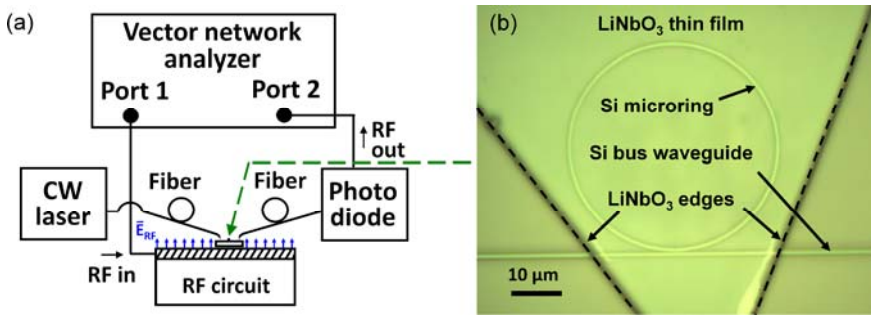

Fig. 13. (a) Measurement setup; (b) Top-view optical micrograph of fabricated electric field sensor.

The measured optical transmission of the electric field sensor is shown in Fig. 14a for 1.3 dBm of input optical power near an optical resonance at 1526.274 nm. The full width half maximum (FWHM) is 118 pm, the free spectral range (FSR) is 5.05 nm, and the extinction ratio is 13.7 dB. The total optical insertion loss is 5.3 dB. The insertion loss is from 4 dB of fiber-to-waveguide coupling loss and 1.3 dB of waveguide transmission loss. The loaded

quality factor is 13,000 and the finesse is 43. The measured optical resonance has a slight asymmetric red shift due to the relatively large thermo-optic nonlinearity in silicon.[24] Figures 14b and 14c show the corresponding values of the microwave VNA S_{21} scattering parameter versus CW laser wavelength. The magnitude of S_{21}, denoted $|S_{21}|$, peaks at approximately -104 dB on the red and blue sides of the optical resonance. Since the thermal nonlinearity is a slow effect compared to the electro-optic effect, the peak RF S_{21} magnitude remains equal on both sides of the optical resonance. At the resonance wavelength, the $|S_{21}|$ is more than 10 dB less than the peak values. The $|S_{21}|$ data is consistent with the steep slopes of the optical transmission near the optical resonance. The phase of S_{21} exhibits a phase change of approximately 180 degrees as the optical wavelength is swept through the resonance, consistent with the sign change in the slope of the optical transmission.

The VNA noise, shown as the dashed red curve in Fig. 14b, is obtained by terminating port 1 of the VNA with a matched 50 Ω load and also connecting the laser directly into the photodiode. As the laser wavelength is swept in time, the VNA noise is recorded. A noise floor of -115 dB is calculated by fitting a Gaussian distribution to the linear magnitude of the noise data. The noise floor is defined as the sum of the mean value of the linear magnitude of the noise and three times its standard deviation.

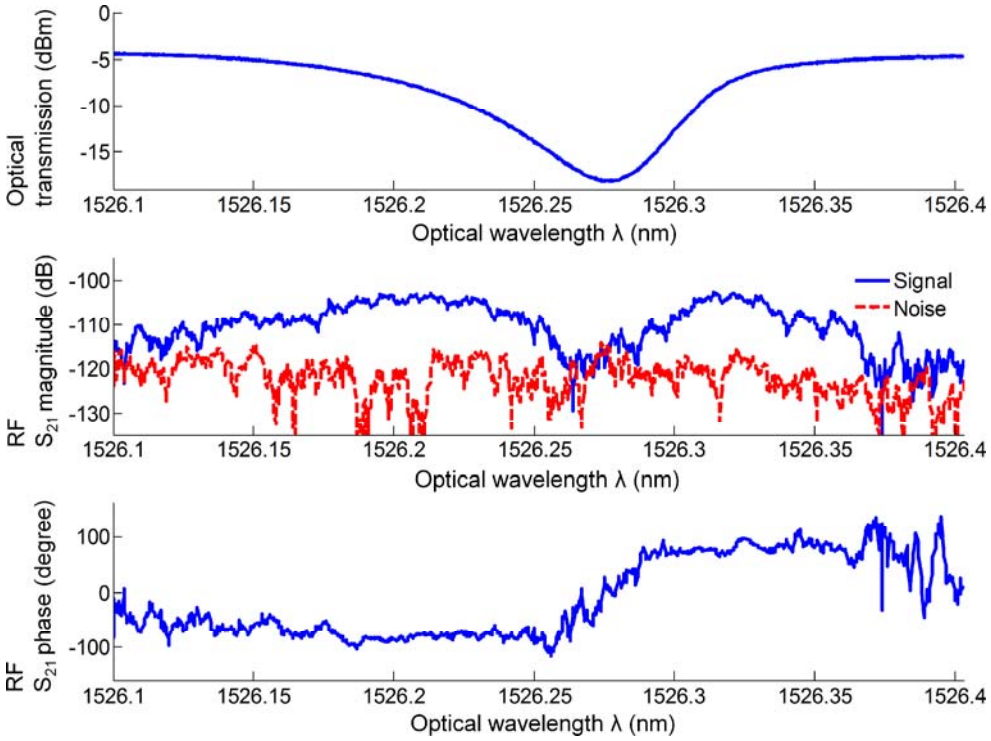

Fig. 14. (a) Measured optical transmission of the electric field sensor; (b) Magnitude of measured microwave VNA S_{21} RF scattering parameter versus CW laser wavelength; (c) Corresponding phase of RF S_{21} versus CW laser wavelength.

As shown in Fig. 14b, there is an 11 dB difference between the peak $|S_{21}|$ and the noise floor. Numerical modeling of the electric field sensor together with the RF microwave circuit is conducted, using the finite element method, to estimate the RF electric field sensitivity.

Since the microwave circuit and the optical thin films composing the sensor differ in spatial dimensions by 4 to 5 orders of magnitude, the GHz varying electromagnetic field in the optical thin films are considered to be quasi-static. Therefore, an approximate two-step modeling procedure is utilized. First, a three-dimensional time-harmonic RF simulation is conducted involving the RF microstrip circuit and the silicon substrate without the optical thin films (*ie.* without the BOX, BCB, patterned silicon waveguide core, $LiNbO_3$, and PECVD oxide). The RF resonance frequency from the simulation is 1.86 GHz and the RF return loss is 6.8 dB, in agreement with the measurements of the RF circuit. The maximum vertical component of the electric field over the top surface of the silicon substrate is then used as an approximate input source field in a static two-dimensional simulation involving only the optical thin films. The small (<3%) effect of the optical thin films on the value of the input source field is neglected. From the simulation, the vertical component of the electric field in the $LiNbO_3$ portion of the sensor, weighted by the optical mode intensity distribution, is found to be 50.8 V/m for an RF input power of 1 mW. From Fig. 14b, reduction of the RF input power by 11 dB produces a signal-to-noise ratio of one. The corresponding RF electric field scales from 50.8 V/m to 14.3 V/m. Based on our system bandwidth of 10 Hz, the demonstrated sensitivity to electric fields is 4.5 V m^{-1} $Hz^{-1/2}$. The sensitivity depends on several factors specific to our experiments. Most notably, the RF signal power entering port 2 of the VNA scales quadratically with input optical power, slope of the resonator optical transmission versus wavelength, photoreceiver conversion gain, and r_{33} in the electro-optic medium.

V. CONCLUSIONS

In this research program, we have investigated the development of a broadband electric field sensor array technology to detect RF electromagnetic energy. We have conducted theoretical analysis, design, fabrication, and test and measurement. Our approach, based on planar electro-optical resonators, was considered to address challenges such as the need for high sensitivity, broad bandwidth, optical modulation without metal electrodes, low reflectivity for wireless signals, scalability to multi-dimensional arrays, high spatial resolution, and low cost.

We have developed sensors based on electro-optic polymers and sensors based on a hybrid material system consisting of silicon and lithium niobate. We conclude that a compact and metal-free hybrid silicon and lithium niobate microring electric field sensor is a promising technology for broadband electric field sensors arrays. The hybrid device combines an ion-sliced lithium niobate thin film with a silicon-on-insulator strip waveguide ring resonator using BCB as an intermediate bonding layer. The sensor has a ring radius of 20 μm and measured loaded quality factor of 13,000 at infrared wavelengths for the quasi-TM mode. The sensor was demonstrated by detecting the fringing electric fields from a microwave circuit operating at 1.86 GHz using a test and measurement setup that incorporates a VNA. The dependence of the magnitude and phase of VNA S_{21} scattering parameter on the optical wavelength is consistent with electro-optic modulation from the lithium niobate portion of the electric field sensor. The demonstrated sensitivity to electric fields is 4.5 V m^{-1} $Hz^{-1/2}$. In comparison, an electric field sensor based on an all-polymer integrated optical electro-optic ring resonator based on disperse red one demonstrated a lower performing sensitivity of 95 V m^{-1} $Hz^{-1/2}$ in a larger footprint.

The conclusions of this research program have advanced the state-of-art in electric field sensors. The results are important for applications including electromagnetic compatibility (EMC) measurements, high-frequency electronic circuit diagnostics, medical equipment field

monitoring, radio-frequency reception, and high power microwave detection. Electric field sensors based on electro-optical technology are advantageous, compared to all-electronic technology, because they can be metal free, compact, and broadband. Furthermore, optical technology is amenable to realizing high spatial resolution sensor arrays and signal routing can utilize fiber optics.

Finally, this research program has opened up new frontiers involving a hybrid material system consisting of silicon and lithium niobate. A hybrid material system consisting of both silicon and lithium niobate enables compact integrated optics on a silicon platform with electro-optic functionality provided by a true second order material susceptibility. The concept is a promising approach to address technological challenges for developing next generation communication systems, sensors, and computers that involve achieving increased power efficiency (energy conservation), while satisfying the concurrent demands for greater bandwidth, enabled by optics, and greater mobility, enabled by wireless techniques and miniaturization.

VI. REFERENCES

1. V. M. N. Passaro, F. Dell'Olio, and F. De Leonardis, "Electromagnetic field photonic sensors," Prog. Quant. Electron. **30**, 45-73 (2006).

2. K. Yang, G. David, J.-G. Yook, I. Papapolymerou, L. P. B. Katehi, and J. F. Whitaker, "Electrooptic mapping and finite-element modeling of the near-field pattern of a microstrip patch antenna," IEEE Trans. Microw. Theory Tech. **48**, 288-294 (2000).

3. V. S. Ilchenko, A. A. Savchenkov, A. B. Matsko, and L. Maleki, "Sub-microwatt photonic microwave receiver," IEEE Photon. Technol. Lett. **14**, 1602-1604 (2002).

4. H. Togo, N. Shimizu, and T. Nagatsuma, "Near-field mapping system using fiber-based electro-optic probe for specific absorption rate measurement," IEICE Trans. Electron. **E90-C**, 436-442 (2007).

5. R. C. J. Hsu, A. Ayazi, B. Houshmand, and B. Jalali, "All-dielectric photonic-assisted radio front-end technology," Nature Photon. **1**, 535-538 (2007).

6. H. Sun, A. Pyajt, J. Luo, Z. Shi, S. Hau, A. K.-Y. Jen, L. R. Dalton, and A. Chen, "All-dielectric electrooptic sensor based on a polymer microresonator coupled side-polished optical fiber," IEEE Sensors J. **7**, 515–524 (2007).

7. K. Okamoto, *Fundamentals of Optical Waveguides*, 2nd ed. (Academic Press, 2006).

8. A. Yariv, "Universal relations for coupling of optical power between microresonators and dielectric waveguide," Electron. Lett. **36**, 321-322 (2000).

9. I. M. White and X. Fan, "On the performance quantification of resonant refractive index sensors," Opt. Express **16,** 1020-1028 (2008).

10. M. Sumetsky, "Optimization of optical ring resonator devices for sensing applications," Opt. Lett. **32**, 2577-2579 (2007).

11. H. C. Song, M. C. Oh, S. W. Ahn, and W. H. Steier, "Flexible low-voltage electro-optic polymer modulators," Appl. Phys. Lett. **82**, 4432–4434 (2003).

12. G. T. Paloczi, Y. Huang, and A. Yariv, "Free-standing all-polymer microring resonator optical filter," Electron. Lett. **39**, 1650–1651 (2003).

13. M. Zhou, "Low-loss polymeric materials for passive waveguide components in fiber optical telecommunication," Opt. Eng. **41**, 1631–1643 (2002).

14. A. Guarino, G. Poberaj, D. Rezzonico, R. Degl'Innocenti, and P. Günter, "Electro-optically tunable microring resonators in lithium niobate," Nature Photon. **1**, 407-410 (2007).

15. H. Hu, R. Ricken, and W. Sohler, "Lithium niobate photonic wires," Opt. Express **17**, 24261-24268 (2009).

16. J. S. Foresi, D. R. Lim, L. Liao, A. M. Agarwal, and L. C. Kimerling, "Small radius bends and large angle splitters in SOI waveguides," Proc. SPIE **3007**, 112-118 (1997).

17. Y. S. Lee, G.-D. Kim, W.-J. Kim, S.-S. Lee, W.-G. Lee, and W. H. Steier, "Hybrid Si-LiNbO3 microring electro-optically tunable resonators for active photonic devices," Opt. Lett. **36**, 1119-1121 (2011).

18. B. G. Yacobi, S. Martin, K. Davis, A. Hudson, and M. Hubert, "Adhesive bonding in microelectronics and photonics," J. Appl. Phys.: Appl. Phys. Rev. **91**, 6227-6262 (2002).

19. F. Niklaus, G. Stemme, J.-Q. Lu, and R. J. Gutmann, "Adhesive wafer bonding," J. Appl. Phys. **99**, 031101 (2006).

20. K. K. Wong, *Properties of Lithium Niobate* (INSPEC, 2002).

21. M. Jazbinšek and M. Zgonik, "Material tensor parameters of LiNbO3 relevant for electro- and elasto-optics," Appl. Phys. B **74**, 407-414 (2002).

22. A. M. Radojevic, M. Levy, R. M. Osgood, A. Kumar, H. Bakhru, C. Tian, and C. Evans, "Large etch-selectivity enhancement in the epitaxial liftoff of single-crystal LiNbO3 films," Appl. Phys. Lett. **74**, 3197-3199 (1999).

23. P. Sun and R. M. Reano, "Cantilever couplers for intra-chip coupling to silicon photonic integrated circuits," Opt. Express **17**, 4565-4574 (2009).

24. P. Sun and R. M. Reano, "Low-power optical bistability in a free-standing silicon ring resonator," Opt. Lett. **35**, 1124-1126 (2010).